Experimental Validation of Multidisciplinary Isoperformance Methodology

Deborah Howell and Olivier de Weck *

Abstract - **Isoperformance is a methodology for predicting contours or n-dimensional surfaces of equal system performance in a trade space composed of design parameters with widely varying bounds. This differs from the traditional point design technique in that a designer can work backwards from a chosen performance level and, using a computer model, can be presented with several different system designs which achieve that level and have a certain cost. By investigating the relationship between contours of isoperformance in model and experiment, modeling rules and error bounds on the computer model can be derived. This will aid greatly in future spacecraft design, especially for space interferometry missions.**

In the first phase of experimental validation of isoperformance a testbed was built that structurally represents a spacecraft, and it was subsequently modelled using finite element techniques. The design parameters that were varied were payload mass, and disturbance level. Using a performance metric based on the spacecraft's displacement, the experimental performance and the predicted model performance were compared. This produced an important insight into the model/experiment relationship: at high disturbance levels, the non-linear structural effects inherent in any physical system caused greater performance prediction errors than at lower disturbance levels.

The second phase of validation involves adding an optical system to the testbed. A 2.75 meter long truss has been added to the testbed, such that light is able to travel along its arms, simulating the travel of light in an interferometer. By expanding the structural model, the testbed more closely resembles a space-based interferometer. Optical elements such as stabilizing breadboards, mirrors, and beamsplitters were then mounted on the truss. These changes have been reflected in the finite element model. The performance of the testbed (the same performance metric as phase one) was measured after the truss was added, and then after the optical elements were placed upon the truss, and was compared to the FEM. Before the truss and optical elements were added, the shape of the frequency response closely resembled that of the FEM, and parametric tuning was required in order to match the frequency responses more exactly. However, with the truss and optical elements mounted on the truss, the structure became sufficiently complex such that the frequency response shapes were quite dissimilar.

Future work includes further alteration of the expanded testbed, a multipoint tuning of integrated optomechanical interferometer models and the usage of pointing and fringe visibility performance metrics.

Keywords - **Isoperformance, Multidisciplinary Design Optimization, Dynamics and Controls, Contour Mapping, Experiment, Space Interferometer**

Introduction

$\mathbf{I}$N designing complex high-performance technical systems there are typically two conflicting quantities that come into play: resources and system performance. One paradigm fixes the amount of available resources (costs) and attempts to optimize the system performance given this constraint. This has traditionally been one of the main thrusts of multidisciplinary design optimization (MDO) in the past.[32, 36, 38] A fundamentally different paradigm is to constrain the system performance J_z to a desired level $J_{z,req}$ and to find a design (or a family of designs) that will achieve this performance at minimal cost. This methodology we will call *isoperformance*. The fundamental motivation behind isoperformance is that performance-optimal solutions are often overdesigned and too expensive. In essence isoperformance enforces $J_z = J_{z,req}$ as an equality constraint, subject to a numerical tolerance τ. Isoperformance has been described by Jones and Kennedy in the context of human factors engineering.[46–48]

The first step in the isoperformance process is to assemble an integrated multidisciplinary model of the system under investigation. One can then predict the performance $J_z(p_j)$ as a function of multidisciplinary parameters p_j, where $j = 1, 2, \ldots, n_p$. A number of mathematical algorithms for approximating the performance invariant set $p_{iso} \in \mathbf{I}$ have been previously developed by de Weck and Miller[8] given such a model. In the bivariate case, $n_p = 2$, the algorithms are exhaustive search with linear interpolation, gradient-based contour following and progressive spline approximation. Higher dimensional cases require different algorithms to acquire the performance invariant set due to computational cost. This allows the prediction of n_p-dimensional isoperformance contours in a bounded trade space, where $p_{j,LB} \leq p_j \leq p_{j,UB}$. Figure 1 shows the types of contours that can be found in a two dimensional design space.

Isoperformance is only of real value if its ability to predict isoperformance contours in real physical, multidisciplinary systems is well understood. Hence, the purpose of this paper is to provide an experimental validation of the isoperformance methodology. To this end a testbed, representing a simplified space interferometer is modeled, constructed and tested in three phases of increasing complexity, see Figure 2.

The testbed combines a disturbance source, struc-
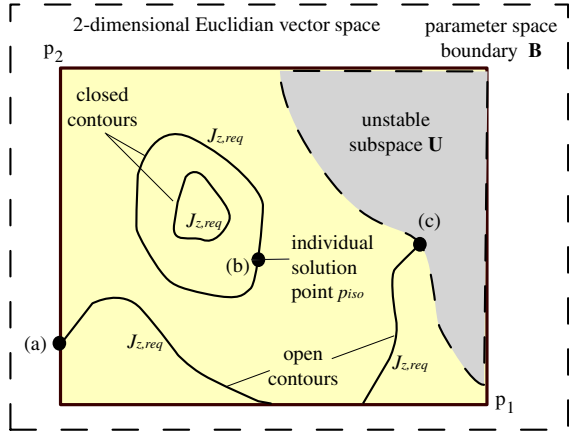
Fig. 1   Isoperformance contours in the bivariate case, $n_p = 2$
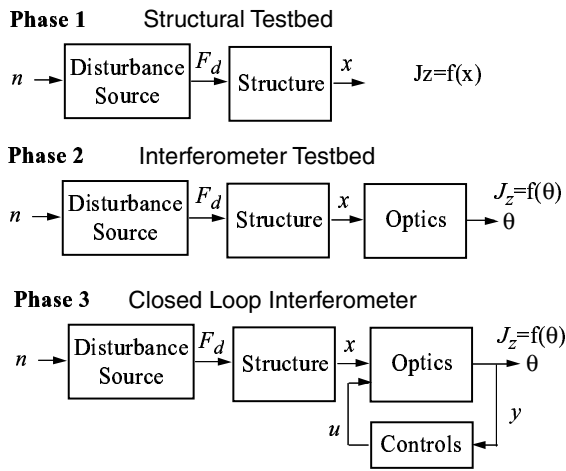
Fig. 2   Three phases of experimental isoperformance validation, where n is colored noise, F_d is the disturbance force, x is structural displacement, θ is wavefront tilt (optical pointing), y is a sensor measurement and u is a control input.

tures, optics and controls. The experimental approach is described below. The objective is to validate isoperformance contours predicted by an integrated model and to understand model-experiment differences due to parametric and non-parametric modeling errors in the different disciplines. This should result in some generalizable conclusions that will assist other researchers in assessing the predictive accuracy of isoperformance contours for their own multidisciplinary systems.

Phase 1 : Structural Testbed Experiment

Phase 1 Structural Testbed Description

The testbed shown in Figure 3 combines a mechanical disturbance source and flexible structure. The main feature of the testbed is that system parameters can be varied over a large range. This is different from the cantilever truss employed by Gutierrez,[17] which was used for physical parameter sensitivity validation

via small perturbations of masses and stiffnesses. The two variable parameters are:

- V_s excitation RMS voltage [V]

- m_p payload mass [lbs]

Figure 3 shows the testbed, which, starting from the top, is comprised of an uniaxial vibration exciter (shaker), with a seismic mass, m_s, driven by a bandpass filtered (0-100 Hz), random noise excitation voltage, V_s. Next the upper stage contains a single small bay of a square truss and a coupling plate. The lower stage consists of a large square truss, a weight bed holding a payload mass, m_p, and an aluminum sandwich base plate. Finally an axial stabilization system and four (4) suspension springs of stiffness k_s complete the arrangement.
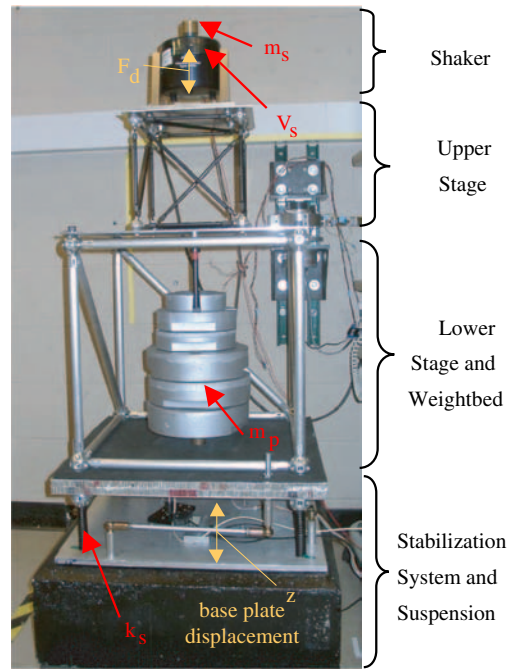
Fig. 3   Phase 1 Structural Testbed

The shaker generates a random axial disturbance force, F_d, whose magnitude and frequency content depend on the excitation voltage, V_s, and the seismic mass, m_s. This device is meant to simulate the disturbances generated by vibrating on-board machinery on a spacecraft (e.g. reaction wheel, cryocooler). The performance is the root-mean-square (RMS) of the base plate displacement x:

$$J_z = E\left[x^T x\right]^{1/2} = E\left[z^T z\right]^{1/2} \qquad (1)$$

This would correspond to jitter of the spacecraft bus in a real space system. The primary instrumentation consists of a uniaxial load cell, which is attached to the seismic mass and measures the disturbance force, F_d.

The performance is measured via an inductive proximitor, which acts as a gap sensor (eddy current gap sensor Bentley XL 5mm). The gap sensor is very sensitive and was calibrated to 0.425 V/mil of displacement with a LB-11/70 Laser Displacement Sensor. The sensor suite below the sandwich plate is shown in Figure 4.
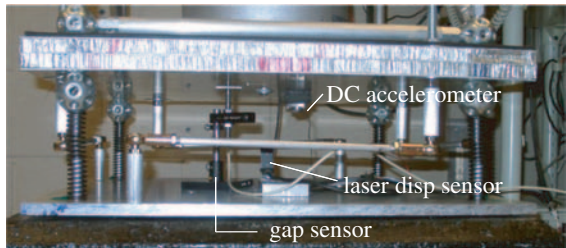
Fig. 4   Phase 1 Testbed Sensors

Phase 1 Experimental Approach

The experimental approach for this phase is presented in Figure 5. First the testbed is assembled, instrumented and calibrated. It was decided to conduct a bivariate isoperformance test, with the performance given by Equation 1. The variable parameters were the excitation voltage, V_s, ranging from 0.1-1.0 [Vrms] as well as the payload mass, m_p, ranging from 0-200 [lbs]. A test matrix was run on the testbed and recorded with parameter increments $\Delta V_s = 0.1$ and $\Delta m_p = 10$, respectively. From this gridded data isoperformance contours were extracted via linear interpolation.[8]
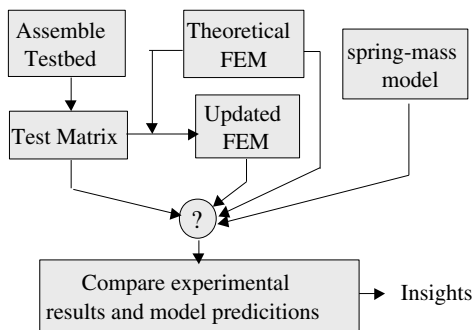
(a) Experimental Procedure

Fig. 5   Experimental Approach

Independently and without knowledge of the experimental results an apriori finite element model (FEM) was constructed ("original FEM"). This model only used assembly drawings, masses from scale measurements and catalogue values for material properties and spring stiffnesses. The predictions from this model would be equivalent to what could be expected from isoperformance analyses for spacecraft in the conceptual and preliminary design phases. A more accurate prediction is expected from an updated FEM, which has its physical parameters tuned such that the FEM and experimental transfer function (measurement model) from F_d to $z = x$ coincide well. Finally

the isoperformance contours are predicted with a single degree-of-freedom (SDOF) model, which lumps the entire testbed mass together with the payload mass m_p over the four suspension springs (in parallel) represented as a single compliance. Insights can be gained by comparing different performance contours for the experiment with the ones predicted for the three models.

Phase 1 Testbed Characterization

The transfer function (FRF) from disturbance (shaker) force to base plate displacement, $G_{zd}(s) = Z(s)/F_d(s)$, where $s = j\omega$, is obtained experimentally and by model prediction, see Figure 6.
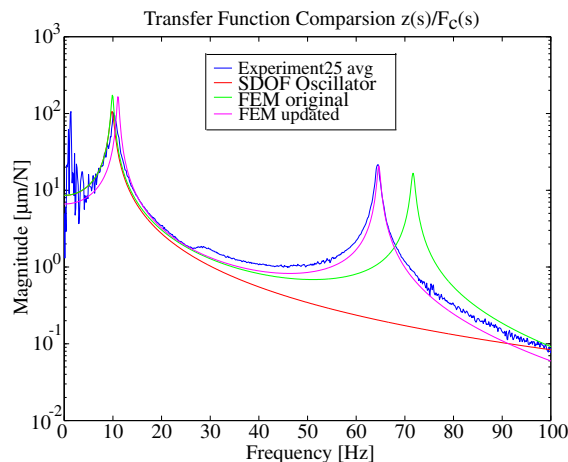
Fig. 6   Transfer Function $G_{zd} = Z(s)/F_d(s)$ **for** $m_p = 0$, $V_s = 1.0$

As can be seen there are two observable modes in the bandwidth up to 100 Hz. The first mode at 10 Hz is the axial base suspension mode, where the testbed translated vertically up and down on the 4 suspension (compression) springs. The second mode at 65 Hz is the upper coupling plate bending mode, which causes a vertical displacement via the center rod. Mode shapes for these two modes are contained in Figure 7.
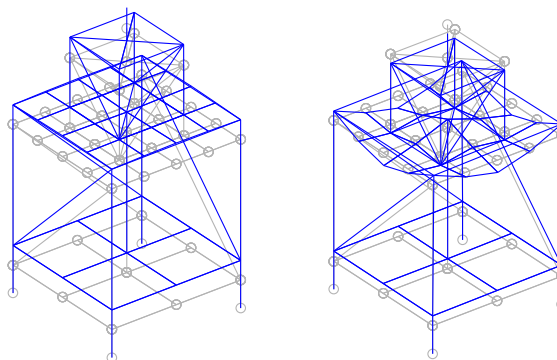
Fig. 7   Structural Testbed Observable Modes (Phase 1)

As expected the SDOF model can only predict the

first resonance. The original FEM overpredicts the upper plate mode by roughly 10 Hz. The updated FEM is the result of manually tuning the material stiffness parameters of the original FEM. The agreement between the updated FEM and the experimental transfer function is very good.

Next the testbed response was investigated as a function of the single parameter m_p. A waterfall plot showing the power spectral density (PSD) of z as a function of m_p is depicted in Figure 8.
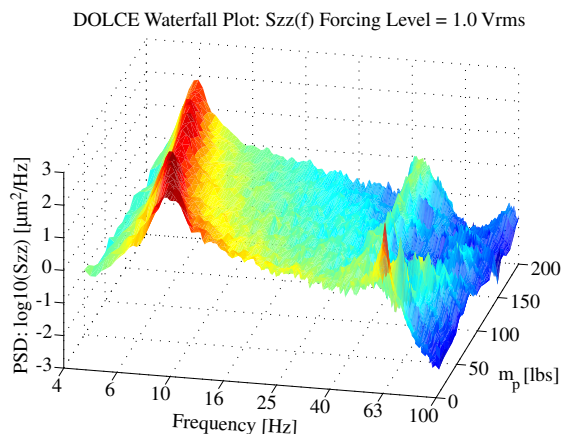
Fig. 8 Waterfall Plot for 1.0 Vrms Forcing Level

It can be seen that the axial suspension mode is dominant for all payload masses. As expected the mode softens with increasing mass from about 10 Hz at $m_p = 0$ [lbs] to 6 Hz at $m_p = 200$ [lbs]. The resonant plate mode at 65 Hz can also be seen, but it is much less clear for larger m_p. A higher frequency mode around 40Hz appears m_p-invariant and we suspect some structural non-linearity. The performance J_z can be computed by integrating under S_{zz} and taking the square root.

$$J_z = \left[2 \int_{f_{\min}}^{f_{\max}} S_{zz}\left(f\right) df \right]^{1/2} \qquad (2)$$

Phase 1 Results and Interpretation

The basis for obtaining the experimental isoperformance contours is the test matrix with V_s and m_p as described under . At each parameter combination the time histories of $F_d(t)$ and $z(t)$, where recorded and the performance $J_z = J_z(V_s, m_p)$ was computed with 25 averages. The results from the test matrix are shown in Figure 9.

The peak displacement RMS value of 57.6 [μm] is obtained for the maximum excitation level ($V_s = 1.0$ [Vrms]) with an empty weight bed ($m_p = 0$ [lbs]). This is intuitively satisfactory, since at this point the maximum disturbance energy enters the system (about 7 N of force F_d RMS), while the disturbability of the system is at a maximum. Recall that the plant transfer function for such a system has a $1/m$ term in the
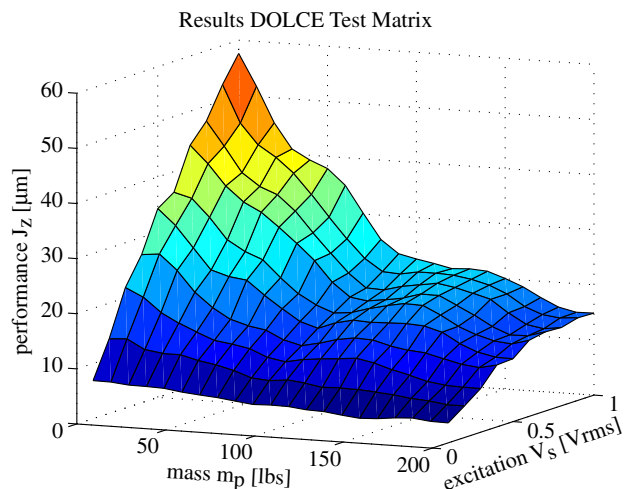
Fig. 9 Phase 1 (V_s,m_p) Test Matrix

numerator. Conversely the lowest response ("best performance") is found for $V_s = 0.1$ and $m_p = 200$. This information is used to obtain isoperformance contours at the 7.5, 15 and 30 [μm] levels (Figure 10).

Comparison of Experimental and Theoretical Isoperformance Contours for DOLCE Testbed

——	Experiment
········	SDOF Model
- - - -	FEM Original
-·-·-	FEM Updated
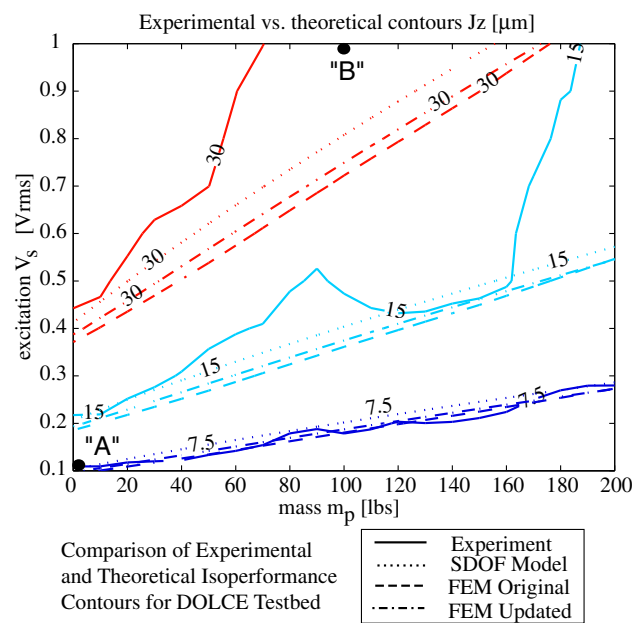
Fig. 10 Phase 1: Comparison of Experimental vs. Theoretical Isoperformance Contours

Similar contours are predicted for the SDOF and FEM's (original and updated). This suggests that the axial suspension mode is dominant in most of the trade space. Excellent correlation between experiment and theory is found at low forcing levels, see the 7.5 μm contour. Deviations are found for larger forcing levels (15 and 30 μm contours), even though the general trends are still predicted correctly by the isoperformance models.

The cause for this deviation is likely due to nonlinear effects in the structural plant as the shaker amplitude increases. To illustrate this statement the

performance PSD's, S_{zz}, have been plotted for the experimental data (blue - solid line) and the FEM prediction (red - dashed line) at two different points in the design space, see Figure 11. Subplot (a) shows the PSD's for point "A" in Figure 10 with $m_p = 0$ [lbs] and $V_s = 0.1$ [Vrms]. Here good agreement between theory and experiment is found. Subplot (b) on the other hand represents Point "B" in Figure 10 which experiences the maximum disturbance level. Figure 11(b) shows that the discrepancy in performance prediction is manly due to the second mode (coupling plate bending). This mode is not visible in the test data and does not contribute to the experimental cumulative RMS. This is due to a non-linear effect, which will have to be investigated in greater detail.
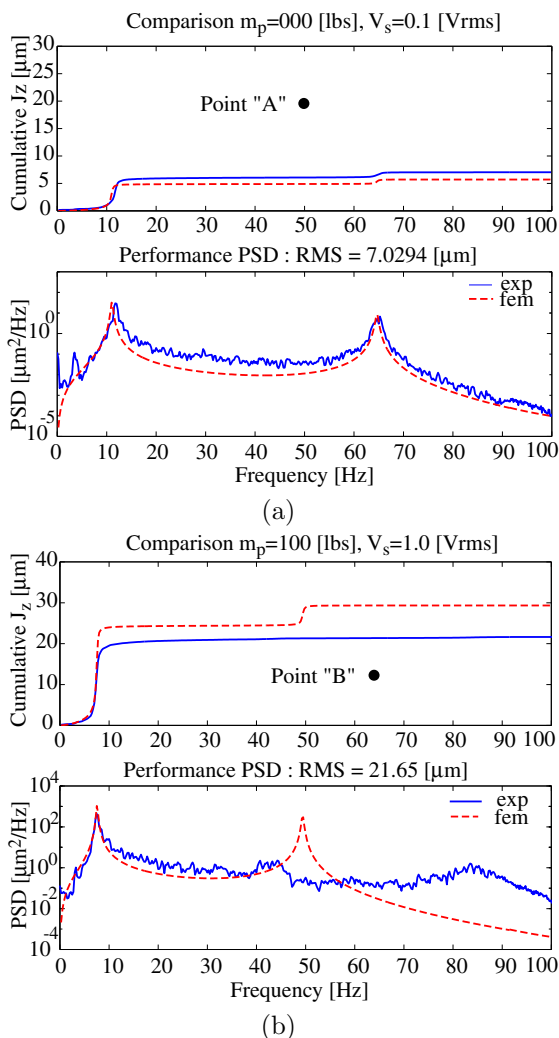
Fig. 11 (a) Comparison of PSD S_{zz} (bottom) and cumulative RMS plot (top) between experiment and FEM prediction for configuration: $m_p = 0$ [lbs], $V_s = 0.1$ [lbs]. Good Agreement. (b) Comparison of PSD S_{zz} (bottom) and cumulative RMS plot (top) between experiment and FEM prediction for configuration: $m_p = 100$ [lbs], $V_s = 1.0$ [lbs]. Poor Agreement.

In conclusion it is found that the isoperformance prediction capability for a purely structural system excited by a mechanical disturbance is good at low disturbance levels, which are representative of the vibration environment on space based opto-mechanical systems. Caution must be exercised if non-linearities are suspected in any part of the system and particularly if performance predictions are to be made at high excitation levels. The next phase adds a truss and Michelson interferometer to the structural testbed.

Phase 2 : Interferometer Testbed Experiment

Phase 2 Structural Testbed Description

A truss and an optical train capable of interferometry are added to the testbed in order to expand the scope of the experimental validation to include optics. In this way, the model will more closely represent space based optomechanical systems, both optically and structurally. Phase 2 will not employ control, but will observe the influence of added optical equipment on structural performance in an open loop system.

The size of the truss was determined by using the finite element method to model an increasing number of bays. Figure 12 shows that when five bays are added to each side of the original testbed, another major mode (90 Hz) is added to the main suspension (10 Hz), and plate (50 Hz) modes. With an additional mode in the observable range (under 100 Hz), the fidelity of our models can be better evaluated.
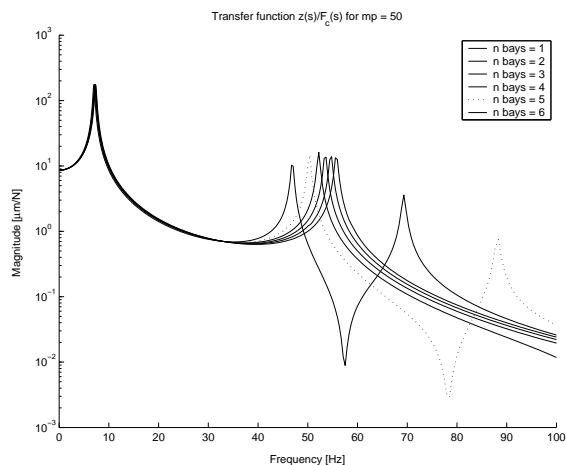
Fig. 12 Phase 2: Performance Predictions

Figures 13 and 14 illustrate the corresponding structural model and testbed for the expanded system with five bays on each side. With the additional bays, the width of the testbed is now 2.75 meters.

The optical train is mounted on the truss and consists of a laser source, beam splitters, mirrors, optical breadboards, and a UNIQ-610 CCD camera (see Figure 15). The laser light is split and sent along each arm of the truss. The CCD camera is located at the center bay, in order capture the two laser beams and record the pointing accuracy. The shaker remains on
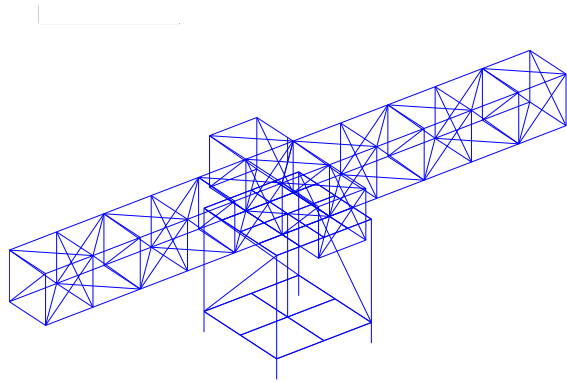
Fig. 13   Phase 2: Structural Model of Expanded Testbed
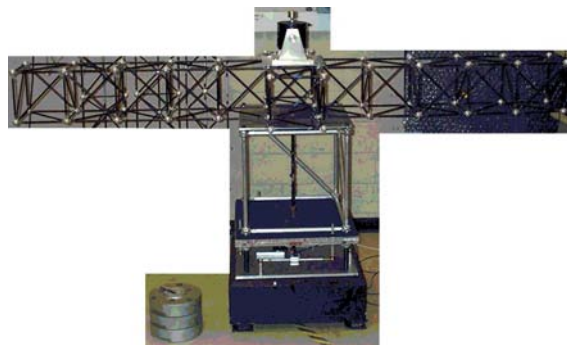
Fig. 14   Phase 2: Expanded Testbed

the testbed, but is now located inside the center bay. The sensors (load cell, gap sensor, laser sensor) and data acquisition system are unchanged. The calibration for the gap sensor has been remeasured and is now 0.348 V/mil.
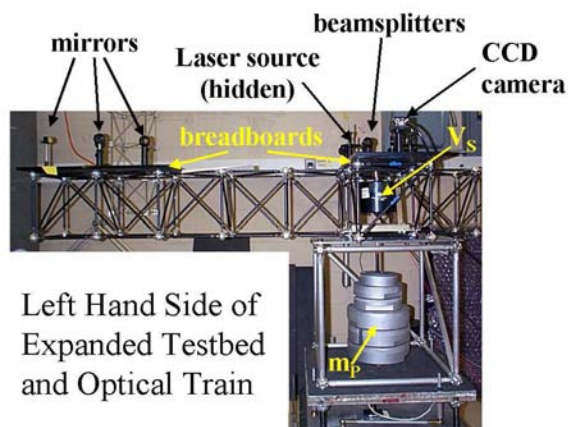
Fig. 15   Left Hand Side of Expanded Testbed and Optical Train

Phase 2 Experimental Approach

The experimental approach for Phase 2 is very similar to that of Phase 1. In order to validate the accuracy of the finite element model, the same performance testing as in Phase 1 is repeated here. Performance testing utilizing the optical metric, pointing accuracy, will be

explored in the future. The two design parameters (V_s excitation RMS voltage [V] and m_p payload mass [lbs]) and the performance parameter remain the same. However, since the performance correlation between experiment and model in Phase 1 was very good only at low forcing levels, the range of excitation voltages, V_s that are explored here are from 0.1-0.5[Vrms]. The parameter increments for this testing are $\Delta V_s = 0.1$ and $\Delta m_p = 50$.

As in Phase 1, an a priori FEM was created (FEM Original), which uses only values that would be available during conceptual and preliminary design phases. An updated FEM was also created, which makes use of the experimental data and changes physical parameter values in order to provide a more accurate performance predictor. An SDOF model was not employed here, since it can only predict the first (main suspension) mode.

Phase 2 Testbed Characterization

The model and experimental frequency response, from disturbance (shaker) force to base plate displacement, can be seen in Figures 16, 17, and 18. It can be seen that the presence of mass has a large effect on the transfer function backbone. Also, there are at least three major modes that can be observed under 70 Hz in each of the figures. As in Phase 1, the first mode (between 5 Hz and 8 Hz) is the main suspension mode. Consistently, the model under-predicts this mode, which could indicate missing mass or a low spring stiffness in the model. It is not immediately clear to which of the experimental modes the second model mode, for $m_p = 0$ (38 Hz) and $m_p = 200$ (28 Hz), should match. This ambiguity complicates and could invalidate the model updating procedure. For this reason, the system configuration for $m_p = 100$ is chosen for model updating. It is clear to which experimental mode the third major model mode belongs (65 Hz, 50 Hz and 49 Hz for $m_p = 0$, 100, and 200, respectively), and it is consistently over-predicted by the model.

The model updating procedure used here is similar to the procedure described in Gutierrez.[17] However, Gutierrez uses an automatic updating algorithm, whereas the one used here is manual. This procedure consists of altering certain physical parameters (within certain bounds) in order to improve the accuracy of the model. The main parameters to be altered are the material stiffness properties. These consist of the Young's moduli (E), the spring stiffness (k), and the damping ratios of the major modes (ζ) . As stated above, the configuration chosen for the model updating has $m_p = 100$ and $V_s = 0.5$. In this configuration, the primary difficulty in model updating is altering the material stiffness parameters in such a way as to shift the second model mode (30 Hz) to the right and shift the third mode (50 Hz) to the left. Figures 19 and 20
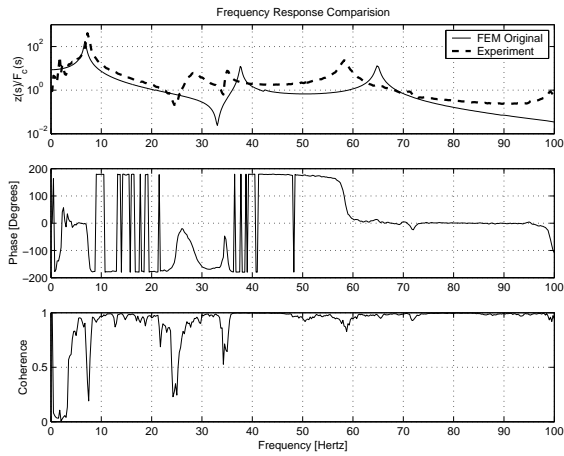
Fig. 16 Model and Experiment Transfer Function $m_p = 0$ **and** $V_s = 0.5$

Fig. 17 Model and Experiment Transfer Function $m_p = 100$ **and** $V_s = 0.5$
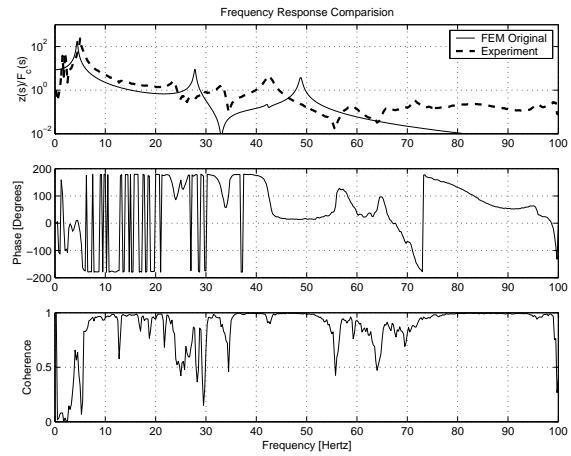
Fig. 18 Model and Experiment Transfer Function $m_p = 200$ **and** $V_s = 0.5$

Fig. 19 Modal Animation: First Flapping Mode
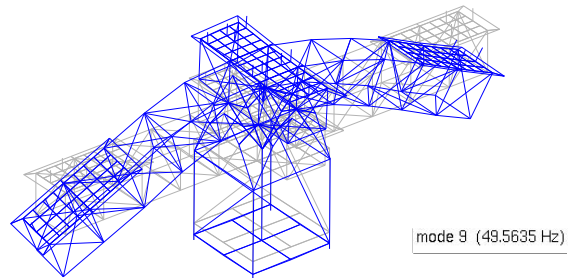
Fig. 20 Modal Animation: Second Flapping Mode

illustrate these mode shapes. These can be described as first and second "flapping" modes. It is expected that flapping modes would be dominant in a system that is disturbed at the center, and that has long cantilevered trusses. These modes may look extremely similar, however, the first flapping mode bends about the center of the truss, whereas the second flapping mode bends about two nodal points on the truss.

In addition to the three major modes shown in the model prediction under 60 Hz, one can see a small shift in the model transfer function at 42 Hz (see arrow in Figure 17). This is a rocking mode (see Figure 21), and is assumed to be virtually unobservable experimentally since the gap sensor and the disturbance force are uniaxial in the z direction. Therefore it is assumed that the 30 Hz model mode represents the 33 Hz experiment mode, and that the 50 Hz model mode represents the 42 Hz experimental mode.

The manual tuning procedure was largely trial and error. The Young's modulus for the small strut was increased in order to move the 30 Hz mode to the right, and the Young's modulus for the solid upper plate was decreased in order to move the 50 Hz mode to the left. The damping ratios apply damping to each detected mode (ζ_1, ζ_2, and ζ_3 match the main suspension, 30 Hz, and 50 Hz modes, respectively) and were altered in order to match the magnitude of each mode. Table 1 shows the changes made to these parameters. In addition, a major increase in the shaker mass was required in order to be able to move the 30 Hz and 50 Hz modes in different directions. This effect occurred since the shaker resides on top of the top solid plate, and this plate has a larger displacement in the 50 Hz mode as compared to 30 Hz mode. Therefore the increase in the shaker mass affected the movement of the 50 Hz mode much more than the 30 Hz mode.

Figure 22 shows the resulting tuned model com-
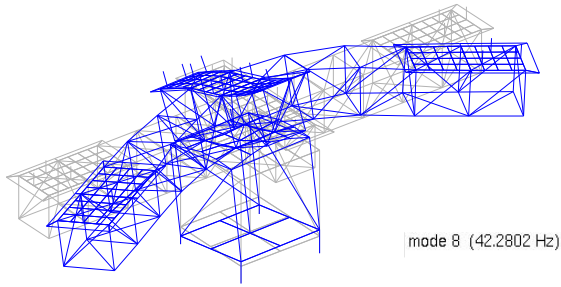
Fig. 21 Modal Animation: Rocking Mode

Parameter	Original	Updated
$E_{SmallStrut}$	72 GPa	75 GPa
$E_{SolidPlate}$	72 GPa	55 GPa
k_{spring}	168 lbs/in	330 lbs/in,
ζ_1	2.5%	1.0%
ζ_2	0.5%	0.3%
ζ_3	0.5%	0.6%

Table 1 Original and Updated Material Stiffness Values

pared with the experimental results and the original model ($m_p = 100$ and $V_s = 0.5$). The placement and the magnitudes of three major modes of the tuned model match well to the experiment. However, at the frequencies between these modes, there is serious mismatch. This could be due to non-parametric modeling error, error in the tuning method, or non-linearities in the structure. As the system becomes more complicated, the rift between model and experiment widens, which is intuitively satisfactory.
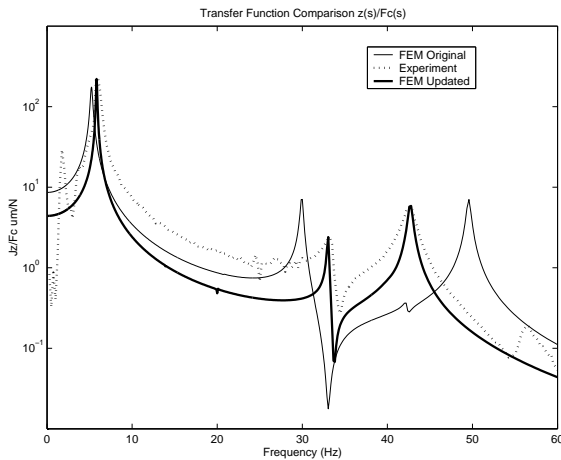
Fig. 22 Model, Experiment, and Tuned Transfer Function $m_p = 100$ and $V_s = 0.5$

Phase 2 Results and Interpretation

The design parameters V_s and m_p were varied, and the performance $J_z = J_z(V_s, m_p)$ computed using the time histories $F_d(t)$ and $z(t)$, as in Phase 1. At $m_p = 0, 50$, and 100, 20 averages were taken, and at $m_p = 200$, 10 averages were taken, due to time constraints. Figure 23 shows these results for the experiment described in Phase 2 Experimental Approach.
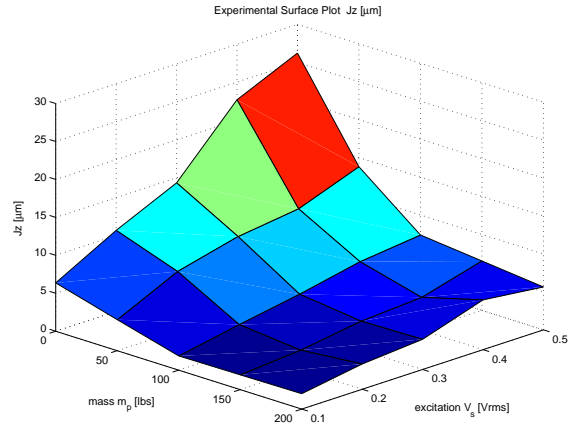
Fig. 23 Phase 2: Experimental Surface Plot of Performance

As in Phase 1, the maximum value of J_z occurs at the highest excitation level $V_s = 0.5$ and the lowest payload mass $m_p = 0$. Also, the minimum value of J_z occurs at the lowest excitation level $V_s = 0.1$ and the highest payload mass $m_p = 200$. Again, this is intuitive.

In order to illustrate the utility of the tuned model, isoperformance contours are shown in Figure 24 at the 7, 10, and 12 [μm] performance levels. It can be seen that the tuned model is actually a worse predictor of performance than the untuned model. In addition, the untuned model is only a good predictor at very low excitation and mass levels (less than 300 Vrms and 60 lbs). This suggests that the effect of non-linearities in the structural plant increases with the disturbance level and the payload mass. The overall trend matches Figure 10 in that the contours generally have positive slopes. This means that in order to maintain the same performance level at a higher disturbance level, the payload mass must also be increased.
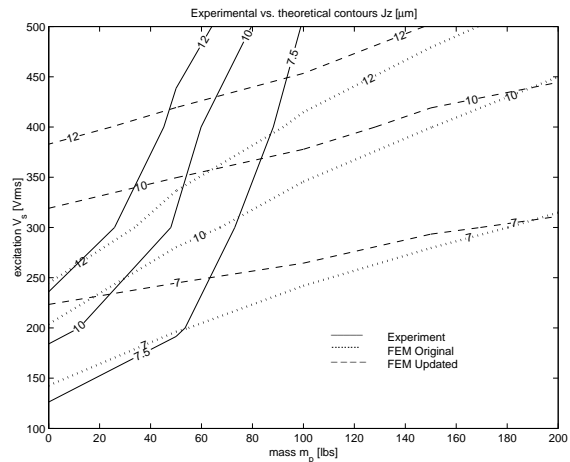
Fig. 24 Phase 2: Isoperformance Contour Comparision

In conclusion, the capability of the isoperformance

contours are shown to be effective in the low excitation range for simple structural systems as in Phase 1. However, if the system's complexity is greatly increased as in Phase 2, the effect of non-linearities, parametric modeling error and non-parametric modeling error are similarly increased, therefore the model must be further refined in order to compensate for these effects.

The second portion of Phase 2 will first change the finite element model in order to more closely resemble the experimental results. Next, an optical performance metric (pointing accuracy, θ), and a new design parameter(optical path length, B) will be employed. The performance can then be compared to a cost function, such as resolution or visibility. The mass and the path length will be varied experimentally and the pointing accuracy will be observed. In this way optical isoperformance contours can be obtained over a wide range of design variables, both experimentally and via optical and structural models.

Phase 3 : Closed-Loop Interferometer Experiment

Phase 3 adds a control loop to the optical system. A general PID control algorithm will be utilized in order to control the fast steering mirrors. The goal of the control algorithm will be to overlap the two beams that are sent to the CCD camera. In this way, the effect of the controller gain on system performance can be evaluated, and isoperformance contours for a closed loop system can be acquired.

Conclusions for general multidisciplinary system

The purpose of this paper is to validate the multidisciplinary isoperformance methodology using a physical interferometer testbed. The experiment is conducted in three phases of increasing complexity. Phase 1 shows that isoperformance contours can be accurately predicted, using a structural (displacement) performance metric and linear time invariant model as long as structural non-linearities are not present. For high excitation amplitudes the linear structural model assumptions break down and the experimental and theoretical contours deviate from each other. Phase 2 adds truss elements and optical components to the setup, and verifies that the structural model is valid within certain excitation and mass ranges. Deviations between theoretical and experimental isoperformance contours in multidisciplinary systems are due to a combination of effects in the disciplinary domains of the underlying integrated system model. Phase 2 is incomplete and in the future it will include an optical metric, pointing accuracy, θ, in order to validate isoperformance. Phase 3 evaluates the predictive accuracy of the isoperformance models with closed loop control. The three phases represent an evolution of a complex opto-mechanical system. At each step, the model of the system is examined, compared to the experimental data, and refined. This step-by-step development of the system model provides not only an accurate model, but also presents insights in to the theoretical-experimental relationship. Once an accurate model exists, isoperformance contours can present the designer with a family of designs that achieve a certain level of performance at minimal cost.

References

[1] K. J. Bathe, *Finite Element Procedures*, Prentice-Hall, Inc., 1996.

[2] B. Bialke, *A compilation of reaction wheel induced spacecraft disturbances*, in Proceedings of the 20th Annual AAS Guidance and Control Conference, Breckenridge, CO, February 5–9, 1997. AAS Paper No. 97-038.

[3] B. Bialke, *A compilation of reaction wheel induced spacecraft disturbances*, 20th Annual American Astronautical Society Guidance and Control Conference, 1 (1997).

[4] R. G. Brown and P. Y. C. Hwang, *Introduction to Random Signals and Applied Kalman Filtering*, John Wiley & Sons, Inc., 1997.

[5] R. Craig Jr., *Structural Dynamics: An Introduction to Computer Methods*, John Wiley & Sons, Inc., 1981.

[6] E. F. Crawley, B. P. Masters, and T. T. Hyde, *Conceptual design methodology for high performance dynamic structures*, in Proceedings of the 36th AIAA Structures, Structural Dynamics, and Materials Conference, New Orleans, LA, April 1995, pp. 2768–2787. AIAA Paper No. 95-2557.

[7] C. de Boor, *A practical guide to splines*, vol. I of Applied mathematical sciences, Springer Verlag, New York, 1 ed., 1978.

[8] O. L. de Weck, *Integrated Modeling and Dynamics Simulation for the Next Generation Space Telescope*, Master's thesis, Massachusetts Institute of Technology, June 1999.

[9] A. Dressler, *HST and Beyond - Exploration and the Search for Origins: A Vision for Ultraviolet-Optical-Infrared Space Astronomy*, vol. 1, Association of Universities for Research in Astronomy, Washington D.C., 1 ed., May 1996.

[10] C. H. Edwards and D. E. Penney, *Multivariable Calculus with Analytic Geometry*, Prentice Hall, Upper Saddle River, NJ 07458, 5 ed., 1998.

[11] C. E. Eyerman and J. F. Shea, *A systems engineering approach to disturbance minimization for spacecraft utilizing controlled structures technology*, MIT SERC Report #2-90, June 1990.

[12] R. L. Fox and M. P. Kapoor, *Rates of change of eigenvalues and eigenvectors*, AIAA Journal, 6 (1968), pp. 2426–2429.

[13] P. R. Freund, *Course Notes 16.910J/6.631 - Introduction to Simulation and Optimization - Massachusetts Institute of Technology*. Module 1, Sep-Oct 1999.

[14] J. J. Gilheany, *Optimum selection of dampers for freely vibrating multidegree of freedom systems*, Proceedings of Damping '89, II (1989), pp. FCC–1:18.

[15] O. Goldreich, *Complexity theory survey*. Internet: http://www.wisdom.weizmann.ac.il, accessed 5-4-2001 2001.

[16] C. Z. Gregory, *Reduction of large flexible spacecraft models using internal balancing theory*, Journal of Guidance, Control, and Dynamics, 7 (1984), pp. 17–32.

[17] H. L. Gutierrez, *Performance Assessment and Enhancement of Precision Controlled Structures During Conceptual Design*, PhD thesis, Massachusetts Institute of Technology, Department of Aeronautics and Astronautics, 1999.

[18] G. J. Hou and S. P. Kenny, *Eigenvalue and eigenvector approximate analysis for repeated eigenvalue problems*, AIAA Journal, 30 (1992).

[19] G. J. Hou and G. Koganti, *Sensitivity analysis of Lyapunov and Ricatti equations with application to controls-structures integrated design*, in Proceedings of the 34th AIAA/ASME/ASCE/AHS/ASC Structures, Structural Dynamics and Materials Conference, LaJolla, CA, April 1993, pp. 1906–1915. AIAA Paper No. 93-1529.

[20] R. N. Jacques, *An approach to the preliminary design of controlled structures*, Master's thesis, Massachusetts Institute of Technology, February 1991. SERC Report #1-91.

[21] Jet Propulsion Laboratory, *Modeling and Analysis for Controlled Optical Systems User's Manual*, 1997.

[22] ———, *Integrated Modeling of Optical Systems User's Manual*, January 1998. JPL D-13040.

[23] H. R. Jr., *Multivariable Calculus with Vectors*, Massachusetts Intitute of Technology, Prentice Hall, Upper Saddle River, New Jersey 07458, 1999.

[24] M. P. Kamat, *Structural Optimization: Status and Promise*, vol. 150 of Progress in Aeronautics and Astronautics, American Institute of Aeronautics and Astronautics, Washington, D.C., 1992.

[25] S. Kenny, *Eigenvalue and eigenvector derivatives for structures*, Final Report, MIT Course 2.093: Computer Methods in Dynamics, April 29,1997.

[26] R. A. Laskin, *SIM Dynamics & Control Requirements Flowdown Process*. Presentation at the SIM Project Preliminary Instrument System Requirements Review, JPL, March 17–18, 1998.

[27] R. A. Laskin and M. San Martin, *Control/structure system design of a spaceborne optical interferometer*, in Proceedings of the AAS/AIAA Astrodynamics Specialist Conference, Stowe, VT, August 1989. AAS Paper No. 89-424.

[28] A. Laub, *Computation of balancing transformations*, Proceedings of JACC, 1 (1980).

[29] A. Laub, M. Heath, C. Paige, and R. Ward, *Computation of system balancing transformations and other applications of simultaneous diagonalization algorithms*, IEEE Trans. Automatic Control, (1987), pp. 115–122.

[30] G. Mallory and D. W. Miller, *Decentralized state estimation for flexible space structures*, 40th AIAA Structural Dynamics and Materials Conference, (1999).

[31] G. J. Mallory, *Development and Experimental Validation of Direct Controller Tuning for Spaceborne Telescopes*, PhD thesis, Massachusetts Institute of Technology, Department of Aeronautics and Astronautics, April 2000. Report SERC 1-2000.

[32] B. P. Masters and E. F. Crawley, *Evolutionary design of controlled structures systems*, in Proceedings of the 38th AIAA Structures, Structural Dynamics, and Materials Conference, Kissammee, FL, April 1997. AIAA Paper No. 97-1263.

[33] A. Messac, R. Gueler, and K. Malek, *Control-structure integrated design: A computational approach*, in Proceedings of the 32nd AIAA/ASME/ASCE/AHS/ASC Structures, Structural Dynamics, and Materials Conference, Baltimore, MD, April 1991, pp. 553–567. AIAA Paper No. 91-1161.

[34] D. Miller, A. Curtis, and O. de Weck, *Architecting the search for terrestrial planets and related origins (astro)*, in SPIE International Symposium on Astronomical Telescopes and Instrumentation 2000, Munich, Germany, 2000.

[35] D. Miller, O. de Weck, S. Uebelhart, R. Grogan, and I. Basdogan, *Integrated dynamics and controls modeling for the space interferometry mission (sim)*, in IEEE Aerospace Conference, Big Sky, Montana, 2001.

[36] M. Milman, M. Salama, R. Scheid, R. Bruno, and J. Gibson, *Integrated control-structure design: A multiobjective approach*, Tech. Rep. D-6767, JPL, October 1989.

[37] M. Milman, M. Salama, R. Scheid, and J. S. Gibson, *Combined control-structural optimization*, Computational Mechanics, (1991), pp. 1–18.

[38] M. Milman, M. Salama, M. Wette, and R. Bruno, *A multiobjective approach to integrated control, struc-ture and optical design*, in Proceedings of the 32nd AIAA/ASME/ASCE/AHS/ASC Structures, Structural Dynamics, and Materials Conference, Baltimore, MD, April 1991, pp. 846–854. AIAA Paper No. 91-1136.

[39] B. C. Moore, *Principal component analysis of linear systems: Controllability, observability, and model reduction*, IEEE Transactions on Automatic Control, AC-26 (1981), pp. 17–32.

[40] D. V. Murthy and R. T. Haftka, *Survey of methods for calculating sensitivity of general eigenproblems*, in Sensitivity Analysis in Engineering, Langley Research Center, September 1986, pp. 177–196. NASA CP 2457.

[41] R. B. Nelson, *Simplified calculations of eigenvector derivatives*, AIAA Journal, 14 (1976), pp. 1201–1205.

[42] S. L. Padula, B. B. James, G. P. C., and S. E. Woodard, *Multidisciplinary optimization of controlled space structures with global sensitivity equations*, Tech. Rep. NASA TP-3130, National Aeronautics and Space Administration, November 1991.

[43] C. G. Park and D. W. Miller, *Structural design and control of high performance optical delay lines*, Master's thesis, Massachusetts Institute of Technology, Department of Aeronautics and Astronautics, August 1995.

[44] J. I. Pritchard, H. M. Adelman, and J. Sobieszczanski-Sobieski, *Optimization for minimum sensitivity to uncertain parameters*, AIAA Journal, 34 (1996), pp. 1501–1504.

[45] D. C. Redding and W. G. Breckenridge, *Optical modeling for dynamics and control analysis*, Journal of Guidance, Control, and Dynamics, 14 (1991), pp. 1021–1032.

[46] M. B. J. Robert S. Kennedy and D. R. Baltzley, *Empirical demonstration of isoperformance methodology preparatory of an interactive expert computerized decision aid. final report*, Tech. Rep. AIAA Technical Library, NTIS HC A03/MF A01, Essex Corporation, Orlando, FL, Feb 1988. AD-A202439; ARI-RN-88-93; Contract: MDA903-87-C-0603; Contract: DA PROJ. 2Q6-65502-M-770.

[47] M. B. J. Robert S. Kennedy and D. R. Baltzley, *Optimal solutions for complex design problems: Using isoperformance software for human factors trade offs*, In NASA. Lyndon B. Johnson Space Center, 2nd Annual Workshop on Space Operations Automation and Robotics (SOAR 1988), N89-19817 12-59 (1988), pp. 313–319.

[48] J. T. R.S. Kennedy and M. B. Jones, *A meta-model for systems development through life cycle phases - coupling the isoperformance methodology with utility analysis*, SAE, Aerospace Technology Conference and Exposition, Long Beach, CA, AIAA Technical Library (1990), p. 9.

[49] J. Spanos, Z. Rahman, and G. Blackwood, *A soft 6-axis active vibration isolator*, in Proceedings of the American Control Conference, Seattle, WA, June 1995.

[50] G. Strang, *Introduction to Applied Mathematics*, Wellesley-Cambridge Press, 1986.

[51] J. Van de Vegte, *Feedback Control Systems*, Prentice-Hall, Inc., 1990.

[52] S. L. Venneri, *Future directions and needs in engineering tools*, ICASE/LaRC/NSF/ARO Workshop on Computational Aerosciences in the 21st Century, (1998). Hampton, Virginia.

[53] M. Wehner, *Personal Communication, TRW , Redondo Beach, CA.*, 1999.

[54] W. T. V. William H. Press, Saul A. Tenkolsky and B. P. Flannery, *Numerical Recipes in C - The Art of Scientific Computing*, Cambridge University Press, 2nd ed., 1996.

[55] P. H. Wirsching, T. L. Paez, and H. Ortiz, *Random Vibrations: Theory and Practice*, John Wiley & Sons, Inc., 1995.

[56] H. N. Yoshikazu Sawaragi and T. Tanino, *Theory of Multiobjective Optimization*, vol. 176 of Mathematics in Science and Engineering, Academic Press Inc., London, United Kingdom, i ed., 1985.

[57] K. Zhou, J. C. Doyle, and K. Glover, *Robust and Optimal Control*, Prentice-Hall, Inc., 1996.